Biomedical Materials

Conditioning of hiPSC-derived cardiomyocytes using surface topography obtained with high throughput technology

To cite this article before publication: Lucas Cortella *et al* 2021 *Biomed. Mater.* in press https://doi.org/10.1088/1748-605X/ac1f73

Conditioning of hiPSC-derived Cardiomyocytes Using Surface Topography Obtained with High Throughput Technology

Lucas R. X. Cortella[1], Idágene A. Cestari[1], Ricardo D. Lahuerta[1], Matheus C. Araña[1], Marcos Soldera[2,3], Andreas Rank[2], Andrés F. Lasagni[2,4] and Ismar N. Cestari[1*]

[1]Bioengineering Department, Heart Institute (InCor), University of São Paulo Medical School, Av. Dr. Enéas de Carvalho Aguiar, 44, 05403-900 – São Paulo, Brazil

[2] Institute for Manufacturing Technology, Technische Universität Dresden, George-Baehr-Str. 3c, 01069 Dresden, Germany

[3] PROBIEN-CONICET, Dto. de Electrotecnia, Universidad Nacional del Comahue, Buenos Aires 1400, 8300 Neuquén, Argentina

[4] Fraunhofer-Institut für Werkstoff- und Strahltechnik IWS, Winterbergstr. 28, 01277 Dresden, Germany

* Correspondence: ismar.cestari@hc.fm.usp.br

Abstract: Surface functionalization of polymers aims to introduce novel properties that favor bioactive responses. We have investigated the possibility of surface functionalization of polyethylene terephthalate (PET) sheets by the combination of laser ablation with hot embossing and the application of such techniques in the field of stem cell research. We investigated the response of human induced pluripotent stem cell-derived cardiomyocytes (hiPSC-CMs) to topography in the low micrometer range. HiPSC-CMs are expected to offer new therapeutic tools for myocardial replacement or regeneration after an infarct or other causes of cardiac tissue loss. However, hiPSC-CMs are phenotypically immature compared to myocytes in the adult myocardium, hampering their clinical application. We aimed to develop and test a high-throughput technique for surface structuring that would improve hiPSC-CMs structural maturation.

We used laser ablation with a ps-laser source in combination with nanoimprint lithography to fabricate large areas of homogeneous micron- to submicron line-like pattern with a spatial period of 3 μm on the PET surface. We evaluated cell morphology, alignment, sarcomeric myofibrils assembly, and calcium transients to evaluate phenotypic changes associated with culturing hiPSC-CMs on functionalized PET. Surface functionalization through hot embossing was able to generate, at low cost, low micrometer features on the PET surface that influenced the hiPSC-CMs phenotype, suggesting improved structural and functional maturation. This technique may be relevant for high-throughput technologies that require conditioning of hiPSC-CMs and may be useful for the production of these cells for drug screening and disease modeling applications with lower costs.

Keywords: hiPSC; cardiomyocytes; surface topography; direct laser interference patterning; roll-to-roll nanoimprint lithography; polyethylene terephthalate.

1. Introduction

Several cell properties are influenced by substrate topography or chemistry, and surface functionalization represents a fundamental step in improving polymer-cell interactions. Nano-and micro-topographic cues can affect cell shape, adhesion, migration, and differentiation, and may introduce novel properties that favor their bioactive response and can determine cell phenotype [1]. Research in this area has intensified in recent years, and new surface structuring techniques have been actively sought. Production cost and scalability are crucial if these strategies are to move from the laboratory to the market. We investigated the functionalization in the low micrometer range of polyethylene terephthalate (PET) sheets by laser ablation and hot embossing, and the application of such techniques in the field of stem cell research. The

response of human induced pluripotent stem cell-derived cardiomyocytes (hiPSC-CM) to microtopography introduced by this relatively low-cost and scalable technique was evaluated with respect to characteristics related to their maturation status.

HiPSC-CMs hold great promise as an autologous cell source for myocardial repair [2]. These cells may allow the production of viable tissue constructs to repair, replace, or augment the function of injured or diseased myocardial tissue. However, hiPSC-derived cardiac constructs have technical limitations that hamper their application in cardiac regeneration, since stem cell-derived cardiomyocytes are phenotypically immature, showing similarities to those in the developing heart [3-5].

When hiPSC-CMs are cultured *in vitro*, they present a random spatial orientation, circular morphology, and an isotropic F-actin organization, which results in an immature contractility pattern [6]. Sarcomeric organization of myofilaments is a hallmark of mature functional cardiomyocytes, and it has been reported that hiPSC-CMs exhibit underdeveloped and disorganized sarcomeres, which, in addition to the lack of t-tubules, results in excitation-contraction coupling properties that are markedly different from those of adult ventricular myocytes [7,8]. Furthermore, sarcomeric α-actinin distribution and sarcomere assemblage are crucial for the functional maturity of cardiomyocytes and have been shown to be altered in iPSCs derived from patients with familial dilated cardiomyopathy [8]. In the native myocardium, CMs are rod-shaped cells that are longitudinally aligned with an anisotropic F-actin distribution that communicates and contracts in a specific directional manner [9]. The proper alignment of cardiomyocytes provides optimal coupling for electrical signal propagation, synchronous cell contractions, and calcium cycling, which are required for efficient cardiac function [10]. Therefore, achieving elongated and oriented hiPSC-CMs as well

as proper organization of sarcomeres and calcium cycling are fundamental goals in cardiac tissue engineering.

Cellular organization similar to adult cardiomyocytes can be achieved *in vitro* by topographical cues that favor cell elongation and alignment. Surface topographies such as anisotropic ridges and grooves in the low to sub-micrometer range may produce such morphological features in different cell types [11-16]. We previously demonstrated that grooves and ridges produced by direct laser interference patterning (DLIP) in the low micrometer range were able to promote elongation and alignment of endothelial cells [17].

DLIP permits the direct fabrication of periodic structures within the low micrometer to nanometer scale on different types of solid materials, such as polymers, metals, and ceramics [18]. This microstructuring technique has significant advantages over other methods, as it is possible to process large areas with reproducibility and accuracy in a single step with throughputs approaching 1 m^2 min^{-1} [19]. Moreover, the DLIP technique can also be employed to structure cylindrical stamps or sleeves, which can be used as masters for roll-to-roll nanoimprint lithography (R2R-NIL). This high-throughput technology allows the production of micro-and nanostructures in a fast and cost-efficient way with potential for industrial applications [20, 21].

In this study, we hypothesized that the surface topography produced by the sequential combination of DLIP and R2R-NIL to structure PET foils will influence myofibrils alignment and calcium handling of hiPSC-CMs and other morphological changes related to cellular maturation. We tested the ability of a line-like pattern of 3 μm spatial period grooves to affect these hiPSC-CMs phenotypic features.

Our results demonstrated that hiPSC-CMs cultured on the microstructured PET presented a more anisotropic morphology and was aligned according to the underlying

grooves. Sarcomeres showed a clear striation pattern of α-actinin and parallel arrangement of the myofibrils F-actin, unspecific myosin light chain-2, and troponin T. Intracellular calcium dynamics obtained from fluorescent signals during spontaneous and electrically stimulated activity presented faster time constants. The sequential combination of DLIP and R2R-NIL can yield a surface processing throughput of 7.5 m^2 min^{-1} on PET foils, making this method adequate for low-cost fabrication and high throughput platforms that may be employed in the production of iPSC-CMs.

2. Methods

2.1. DLIP and R2R hot embossing on PET

Nickel sleeves with a thickness of 200 µm, 300 mm width, and 300 mm diameter (Saechsische Walzengravur GmbH, Germany) were structured by DLIP. The initial surface roughness is 61 nm. Prior to laser processing, the sleeve was cleaned with ethanol. The nickel sleeve was structured on a 3D-DLIP unit employing a rotary axis system (developed at the TU-Dresden). The 3D-DLIP structuring system utilizes a solid-state ps-laser with a 1064 nm laser wavelength (Edgewave PX200, Germany) with a pulse duration of 10 ps. Line-like structures with a spatial period of 3.0 µm were produced by employing a pulse-to-pulse feed of 40 µm, a spot diameter of 190 µm, and a single pulse laser fluence of 0.56 J cm^{-2}. Further experimental details can be found elsewhere [22, 23].

To obtain a hydrophobic surface on the Ni sleeve and avoid sticking of the polymeric foil [24], the sleeve was covered with a self-assembled monolayer (SAM) based on phosphonic acid derivatives (1H,1H,2H,2Hperfluoro-n-decylphosphonic acid and 1H,1H,2H,2H-perfluoro-noctylphosphonic acid dissolved in isopropanol at a molar concentration of 2 mmol L^{-1}). After immersion for one hour in this solution, the sleeve

was rinsed with isopropanol and dried in an oven at 150 °C for 10 min. Static water contact angle (WCA) measurements were performed on DLIP-treated Ni samples with and without the SAM using a contact angle system (Dataphysics OCA-20, Germany) under ambient conditions with deionized water.

A 200 µm thickness and 250 mm width foil of polyethylene terephthalate modified with cyclohexane dimethanol (PET-G, Pütz Folien GmbH+Co. KG, Germany) was used as the substrate in the hot-embossing process. A roll-to-roll nanoimprint lithography system (R2R Basecoater BC51, COATEMA, Germany) with roller diameters of 299.077 mm and a width of 300 mm was utilized. The R2R-system allows web speeds between 1 m min^{-1} and 50 m min^{-1}, pressures of up to eight bars, and separate heating of the bottom and top rollers. The PET-G foil was imprinted at a pressure of six bar resulting in a force of 29.5 kN. The top roller was used to imprint the polymer foil at a depth of 15 µm. Considering these values, a pressure of 90.6 MPa was applied to the foil. The temperatures of the top and bottom rollers were kept constant at 75 °C and 45 °C, respectively. The web speed was set to 30 m min^{-1}.

2.2. DLIP-R2R-modified PET surface characterization – atomic force microscopy (AFM), scanning electron microscopy (SEM), and wettability analysis

The surface micropattern produced on PET was characterized by AFM with a Nanoscope IIIA (Digital Instruments, USA), and the measurements were conducted in tapping mode. The aspects measured were spatial period, defined as the distance between the center of two consecutive ridges; groove depth, which was measured from ridge top to groove bottom and ridge width, determined as full width at half maximum of groove depth [25].

The topographies were further visualized using a TM 3000 scanning electron microscope (Hitachi, Japan) at an accelerating voltage of 5 kV. Samples were cut into 5.5 mm round pieces, cleaned with 70% (v/v) ethanol, and dried at room temperature before SEM visualization.

Contact angle measurements were performed with a Drop Shape Analyzer model 100 (Krüss, Germany) goniometer and the Advance software using the sessile drop method. The wetting behavior values were obtained by measuring the static contact angle of droplets of deionized water (0.75 µl) on the surface of unmodified, DLIP-R2R-modified, and Geltrex-treated PET samples. The contact angle data of 20 measurements per sample were averaged and expressed as mean ± standard deviation.

2.3. HiPSC-CMs cell culture on DLIP-R2R-modified PET

HiPSC-CMs were purchased from Pluricell Biotech (São Paulo, Brazil) as a fully differentiated lineage at the 15th day after the start of differentiation and cultivated following the manufacturer's instructions. Cells were plated on 24-well plates (Sarstedt), previously coated with Geltrex (A14133-01, Thermo Fisher), which is a soluble form of basement membrane matrix extracted from murine tumors. Geltrex coating was performed following the manufacturer's instructions for the thin gel method (non-gelling), which produces a protein layer on the surface. First, Geltrex was diluted 1:100 with an appropriate volume of pre-chilled (4 °C) RPMI medium (1% final concentration) and kept at 4°C until use. Coating was obtained by adding sufficient diluted Geltrex solution to cover the entire growth surface area. After two hours at 37 °C, the solution was aspirated and the cells were immediately seeded at a seeding density of 137 × 10^3 cm^{-2} and cultured at 37 °C in a 5% CO^2 atmosphere with RPMI (Thermo Fisher) medium supplemented with plating medium supplement

(PluriCardio™ PMS). Culture medium was replaced with RPMI containing maintenance medium supplement (PluriCardio™ MMS) every 24 h.

Prior to the experiments, unmodified and DLIP-R2R-modified PET samples were cut in 5.5 mm diameter circles, washed in an ultrasonic bath (Elma, Germany), immersed in 70% (v/v) ethanol for 30 min, and subsequently dried under UV light for 40 min. Samples were placed inside a 96-well microplate (Sarstedt) and coated with Geltrex solution at 37 °C for two hours prior to cell seeding. HiPSC-CMs were harvested from the 24-well plate with 0.35% trypsin/EDTA solution (Gibco), centrifuged at 250 × g for 5 min, suspended in RPMI with PMS, and seeded onto pre-coated PET at a density of 17×10^3 cm^{-2}, 34×10^3 cm^{-2}, and 14×10^4 cm^{-2} for morphology and orientation analysis, immunocytochemistry assays, and intracellular calcium fluctuation measurements, respectively. The culture medium was replaced with RPMI containing MMS every 24 h during the experiments. The experimental groups were defined as follows: (a) unmodified PET (control) and (b) PET-L3 (line-like pattern featuring a spatial period of 3 μm).

2.4. Cell morphology and orientation – SEM and fluorescent staining of F-actin

The influence of topographical micropattern on hiPSC-CMs morphology and alignment was investigated. Cells at 19th day after differentiation were cultured on unmodified or DLIP-R2R-modified PET for two days and fixed with 4% paraformaldehyde (PFA) (Sigma) for one hour at 4 °C, washed with phosphate buffered saline (PBS) (Gibco), and dried at room temperature (RT) before being viewed under a scanning electron microscope under vacuum condition.

F-actin myofibrils were visualized by fluorescent staining using a fluorescence microscope (TM300, Nikon, Japan) equipped with an AxioCam MRC camera (Zeiss,

Germany). Cells were fixed with 4% PFA in PBS for two hours at 4 °C, permeabilized with 0.1% Igepal (Sigma, Brazil) at 37 °C for 30 min, and blocked with 2% bovine serum albumin (BSA) (Sigma, Brazil) in PBS for one hour. F-actin fibers were stained with alexa-488-phalloidin (A12379, Life Tech., USA) at 1:100 in 2% BSA/PBS. PET samples were maintained in PBS/glycerol (1:1) solution and protected from light prior to fluorescence microscopy analysis.

SEM and fluorescent images were used to evaluate cell morphology with ZEN 2012 software (Zeiss, Germany), and cell orientation was performed using Image J (NIH, USA). Six samples from each experimental group were examined, and at least 150 cells per sample were imaged. Based on the outline of isolated cells, we estimated the values of spreading area (filled region by projected cell boundary) and aspect ratio, which gives an indication for cellular elongation and circularity index (CI). The aspect ratio is defined as the ratio between the breadth (minimum feret) and length (maximum feret) of each cell and varies from zero to one. Circularity provides an indicator of cell morphology by quantifying the irregularity in the cellular shape, where $CI = (4\times\pi\times area)(perimeter)^{-2}$. For the aspect ratio and circularity index, a value of 1 approximates the shape of a circle, and a value of zero indicates that of a straight line.

Cell orientation was determined by measuring the angle between the major axis of the cell and the axis of the micropatterned grooves, and they were considered aligned when this angle was lower than 10°. A minimum angle of 0° indicated parallel alignment from the groove axis; a maximum angle of 90° suggested perpendicular alignment, and an average angle of 45° was expected for random orientation. For quantification of cell orientation in the control, an arbitrary axis was selected.

2.5. Immunocytochemistry – troponin T; sarcomeric alpha-actinin; unspecific myosin light chain-2 (MLC-2)

Cells at 29th day after differentiation were seeded on unmodified or DLIP-R2R-modified PET and cultured for five days before being fixed with 4% PFA for one hour at 4 °C, washed twice with PBS, and permeabilized with 0.1% Triton X-100 (Sigma) for 30 min at RT. Cells were then blocked with a blocking solution (10% goat serum/0.1% Triton X-100 / PBS) for 20 min at RT and incubated with anti-troponin T (mouse) (Abcam 8295) at 1:200; anti-α-sarcomeric actinin (mouse) (Thermo 22863) at 1:100 and anti-MLC-2 (rabbit) (Abcam 79935) at 1:200 in 1% BSA/PBS overnight at 4 °C. Cells were incubated with secondary antibodies goat-antimouse Alexa-488 and goat-antirabbit Alexa-488 at 1:200 in 1% BSA/PBS for two hours protected from light at RT, and maintained in 1:1 PBS/glycerol solution prior to fluorescence microscopy analysis. Immunostained sarcomeric alpha-actinin images were used to estimate sarcomere length using ZEN 2012 software, and at least 80 sarcomeres were measured for each experimental group.

2.6 Calcium transients

Spontaneous and electrically stimulated contractile activities of hiPSC-CMs were assessed by measuring the Ca^{2+} fluorescence signal. The kinetic parameters analyzed were time-to-peak (t_{peak}), decay time (dct), peak width at 50% (pw_{50}), and decay rate (τ). Cells at 29th day were seeded on unmodified or DLIP-R2R-modified PET and cultured for 20 days until used in the Ca^{2+} fluctuation experiments. Spontaneous and triggered activities were recorded using the fluorescent dye Fluo-4. Cells were loaded with 5 μM Fluo-4 (ThermoFisher) diluted in Hank's balanced salt solution (HBSS) containing 0.2% Pluronic F-127, 20 mM HEPES and 2.5 mM probenecid for 45 min at 37 °C. Before recording the fluorescence signals, cells were washed with indicator-free RPMI-MMS

medium (with 20 mM HEPES and 2.5 mM probenecid) and incubated for a further 30 min to allow complete intracellular de-esterification.

HiPSC-CMs cultivated on PET were transferred to the cell chamber and kept at 36.5 °C ± 0.5 °C using a conductive indium tin oxide sheet (60 Ω / cm², Sigma, 639303) attached to the bottom of the chamber. During the experiments, cells were perfused with a washing medium at 30 μL s^{-1}. Electrical stimulation was done using a modified C-Stim Chamber System (IonOptix®, USA) and platinum electrodes connected to a MyoPacer Stimulator (IonOptix®, Milton, USA) [26; Matheus, CBEB 2020]. Cells were paced using a field stimulator with a positive monophasic pulse (2 ms, 3 Hz, 5 V).

For data collection, the fluorescent signal was captured by an RTE/CCD-1300-Y/HS camera (Princeton Instruments, USA) adjusted to a resolution of 64 × 64 pixels and an exposure time of 10 ms, with a frame rate of 30 frames per second. A MicroMAX Controller (Princeton Instruments, USA) was connected to the camera, and data post-processing was performed using the WinView/32 software (Princeton Instruments, USA) to generate visual maps of light intensity. Recordings were obtained from three distinct regions of the hiPSC-CMs culture repeated three times.

Signals were collected and analyzed with an automated script routine implemented in Python 3.8 programming language using the scientific numerical libraries Numpy, Scipy, and Matplotlib [27, 28, 29] to map the luminous intensity levels in each pixel of each captured frame. The observations of the average luminous intensity levels through the time domain n can be represented in the form of single-exponential dynamics [30], given by the following exponential decay function:

$$f(t_i, A_0, \tau) = A_0 e^{-\tau t_i}$$

where the parameter A_0 is equal to the value at time $t_0 = 0$, e is Euler's constant, and τ is a constant that determines the rate of decay. Therefore, the fitting should approximate

the data closely, approximate the selected function $f(t_i,A_0,\tau)$ over a finite range in the time domain t_i and the exponential form possesses strongly non-orthogonal properties [30]. The fit of a model to the data found by observation is measured by its residual r_i, defined as the difference between the actual value of the dependent variable y_i and the value predicted by the exponential decay function:

$$r_i = y_i - f(t_i,A_0,\tau)$$

The least-squares method finds the optimal parameter values by iteratively minimizing the sum of the squared residuals:

$$Min\sum_{i=0}^{n}\frac{1}{2}(r_i)^2 \quad , \quad A_0,\tau \in \mathbb{R}^+$$

The particular form used in this study is based on Levenberg-Marquardt, which is effective and numerically stable for nonlinear curves [31, 32].

2.7. Statistical analysis

All values were obtained from the datasets of three independent experiments performed in duplicate. Statistical comparison between DLIP-R2R-modified PET and unmodified PET groups was performed using the Mann –Whitney rank sum test using SigmaStat statistical software (Jandel Scientific). Statistical significance was set at $P < 0.05$. Data are expressed as the mean ± standard deviation (SD).

3. Results

3.1 *DLIP and R2R-NIL on PET – Surface characterization - AFM, SEM and wettability analysis*

The hydrophobic surface of the Ni sleeve after the previous treatment with SAM was confirmed by WCA measurements. The WCA of the Ni sample increased from 70° ± 5° when no SAM was applied to 130° ± 5° after covering the sample with the SAM.

A two-beam configuration in the 3D-DLIP system was used to fabricate well-defined and homogeneous line-like micropattern consisting of periodic and parallel ridges and grooves on the metal sleeves. After using DLIP to create the master stamp, we used R2R-NIL to produce a line-like pattern with these geometric features in a PET foil and investigated how hiPSC-CM responded to this microstructured substrate.

Figure 1 (A) displays a 3D projection from the AFM image of the surface micropattern from structured PET, and Figure 1 (B) schematically represents the topographical features measured by AFM. Ridges were fabricated with 3 ± 0.02 µm of periodicity, 2 ± 0.04 µm of width and 1 ± 0.01 µm of groove depth.

The micropattern was also visualized by SEM at different magnifications (Figure 2 (B), (C), and (D)). A PET sheet, as received from the supplier and without any imprint treatment, was used as the control group (Figure 2 (A)).

The wetting behavior of the PET samples was characterized using contact-angle measurements. Unmodified and patterned PET exhibited hydrophilic surfaces with contact angles of 80.4 ± 0.8° and 88.0 ± 1.0°, respectively. Geltrex-coated PET samples showed a decrease in contact angles, resulting in 61.9 ± 0.6° and 63.1 ± 0.7° for control and patterned PET, respectively.

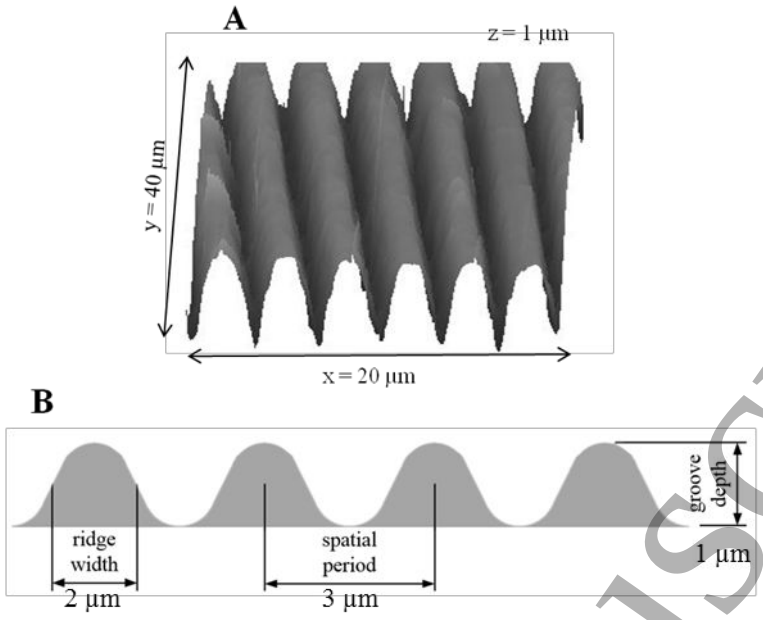

Figure 1. (A) AFM characterization of the surface micropattern produced on PET represented by 3D projection obtained with NanoScope Analysis software. The X and Y axes indicate width and length of the sections, respectively. Note that Z-axis is expanded for better visualization (aspect ratio = 0.4). (B) Schematic representation of the topographical features measured by AFM and their respective values.

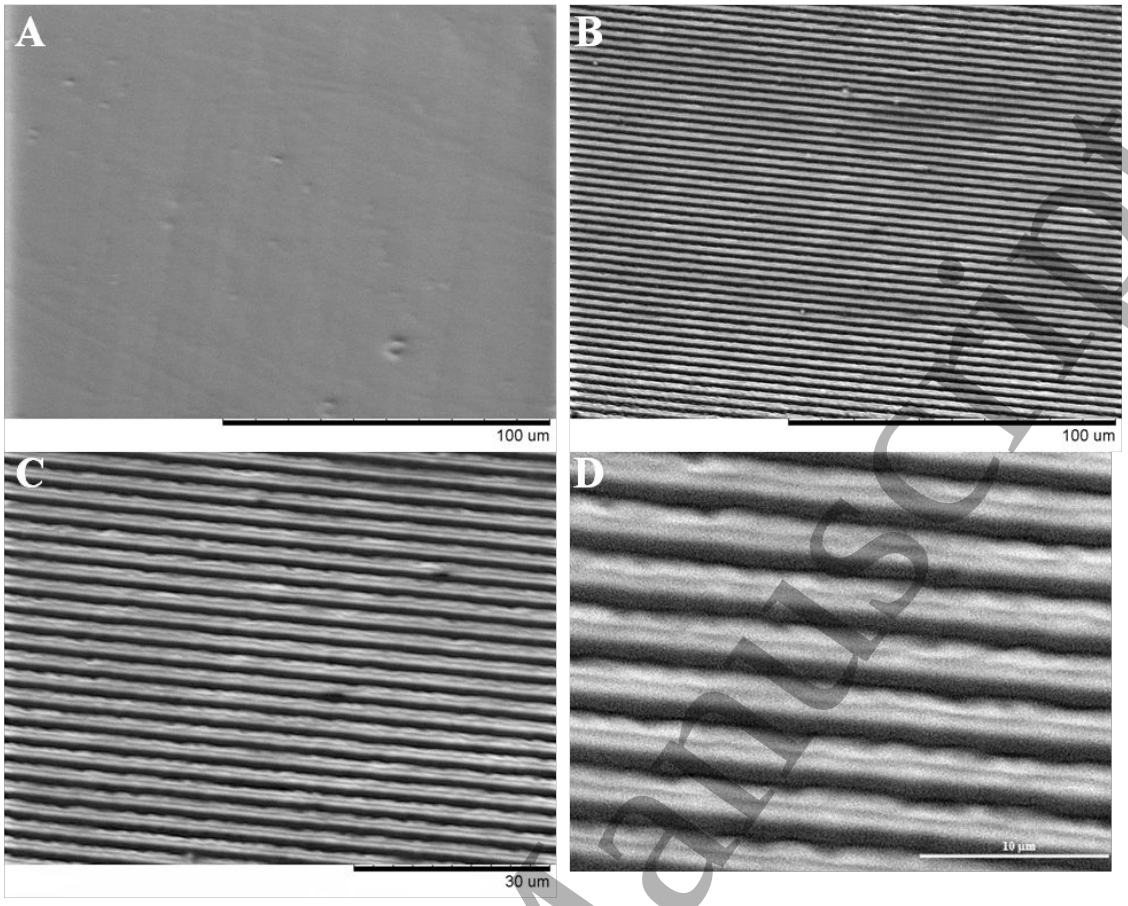

Figure 2. Visualization by SEM of non-modified PET (A) and the surface micropattern produced on PET sheet under different magnifications (B), (C) and (D). Scale bar: (A), (B) 100 µm; (C) 30 µm and (D) 10 µm.

3.2 Alignment of hiPSC-CMs in response to DLIP-R2R-modified PET

Figure 3 shows the distribution of orientation angles of hiPSC-CMs cultured on DLIP-R2R-modified PET and the control. Table 1 summarizes the average values of the orientation angle and the percentage of aligned cells. HiPSC-CMs cultured on non-patterned PET were randomly orientated, resulting in an expected mean angle of 43 ± 24°. In contrast, the interaction of hiPSC-CMs with the topography narrowed the distribution of orientation angles, with approximately 70% of cells within zero to 20° (Figure 3). Almost 50% of cells aligned to the grooves at angles lower than 10° and 90% were oriented within zero to 50° from the groove direction. Figure 4 (B) and (D)

illustrate the differential behavior of the cells onto micropatterned PET with respect to orientation, showing most hiPSC-CMs following the groove direction, whereas cells on non-patterned surface (Figure 4 (A) and (C)) did not exhibit any detectable preferential direction, as shown by the histogram from the control group (Figure 3).

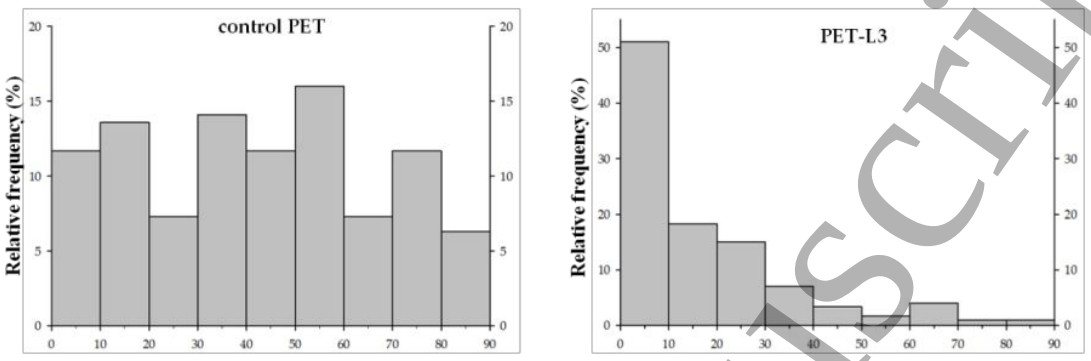

Figure 3. Histograms report the distribution of orientation angles in degrees (x axis) and their relative frequency (%) (y axis) of hiPSC-CMs cultured on control (left) or DLIP-R2R-modified PET (right).

Table 1. Mean orientation angles and percentage of aligned cells on micropatterned PET and control. Cells oriented with angle lower than 10° in relation to the groove direction were considered aligned. (*) indicates statistical significance ($P < 0.001$) between groups.

	mean orientation angle (°)	% aligned cells (< 10°)
Control PET	43	12
PET-L3	10 *	51 *

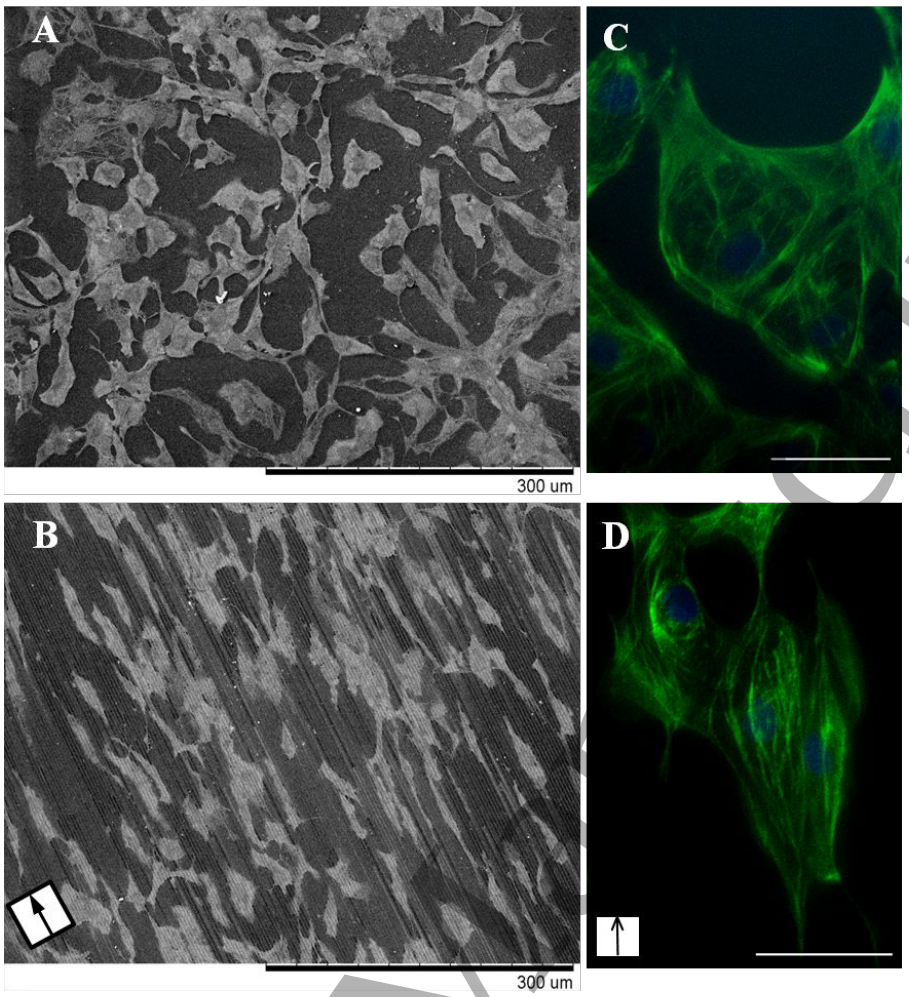

Figure 4. SEM images (left) and fluorescent staining of F-actin (right) showing distinct morphology and alignment between hiPSC-CMs grown on control PET (A, C) or DLIP-R2R-modified PET (B, D). Scale bars: (A), (B) 300 μm; (C), (D) 50 μm. The arrow inside the box indicates the direction of the grooves.

3.3 *Differential morphology of hiPSC-CMs cultured on DLIP-R2R-modified PET – aspect ratio, circularity index and area*

The aspect ratio, circularity index, and cell area are important structural features present *in vivo* [33] and *in vitro* [34] and were thus evaluated. HiPSC-CMs responded to the micropatterned surface by adopting a more elongated shape than cells in contact with non-patterned PET, showing a 34% difference ($P < 0.001$) in aspect ratio (Figure

5). The circularity index (Figure 6) and spreading area (Figure 7) from cells on DLIP-R2R-modified PET also showed an 11% and 29% reduction ($P < 0.001$), respectively, compared to the control.

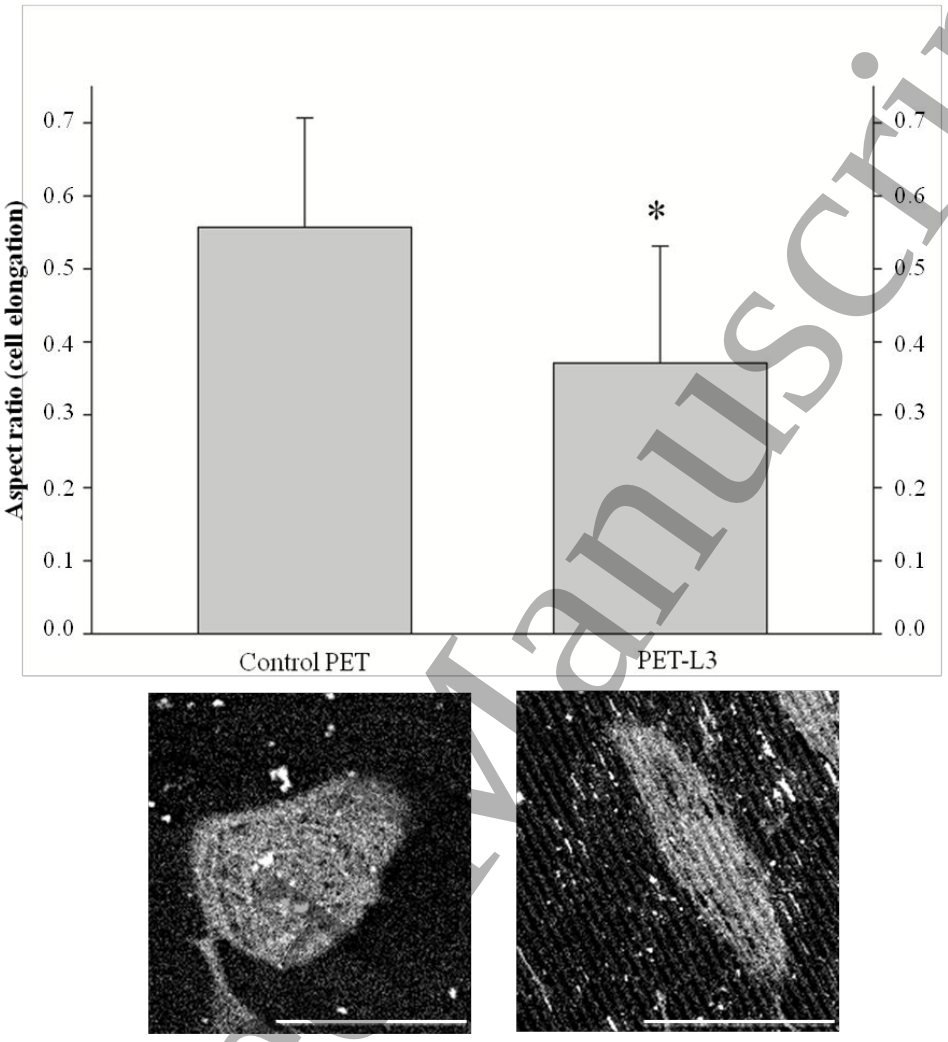

Figure 5. Top: aspect ratio (elongation) from hiPSC-CMs cultured on control or DLIP-R2R-modified PET. (*) indicates statistical significance ($P < 0.001$) between groups. Bottom: SEM images showing isolated hiPSC-CM exhibiting a more elongated shape in response to structured PET (right) compared to non-modified PET (left). Scale bar: 50 µm.

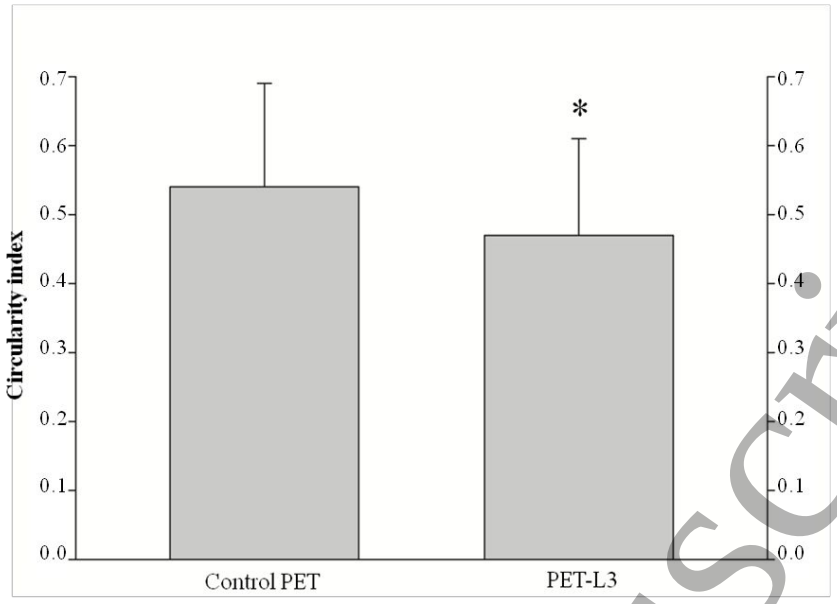

Figure 6. Circularity index from hiPSC-CMs cultured on control or DLIP-R2R-modified PET. (*) indicates statistical significance ($P < 0.001$) between groups.

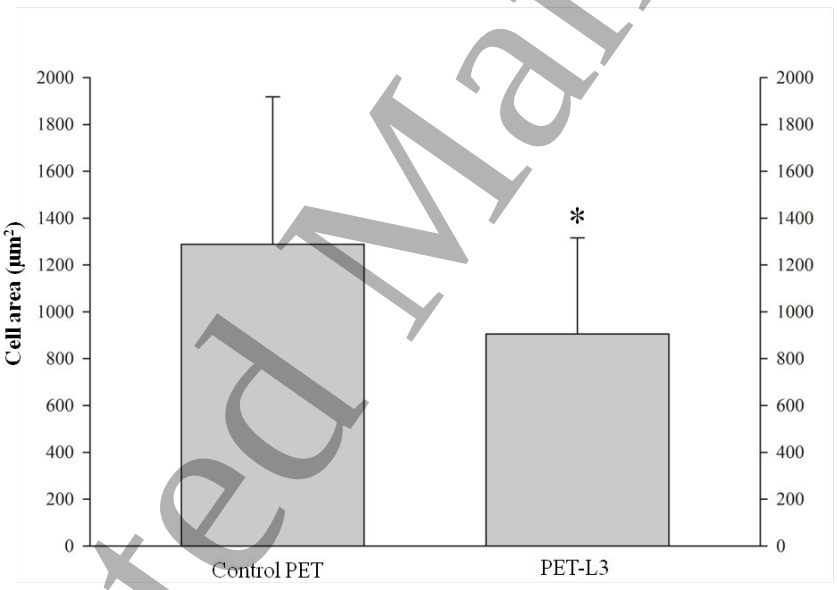

Figure 7. Spreading area (μm²) from hiPSC-CMs cultured on control or DLIP-R2R-modified PET. (*) indicates statistical significance ($P < 0.001$) between groups.

3.4 *Myofibrils alignment – troponin T, F-actin, myosin light chain-2 and sarcomeric α-actinin*

In relation to myofibrils assembly, hiPSC-CMs cultured onto the micropatterned PET exhibited anisotropic organization in response to the topography. F-actin and myosin light chain-2 were assembled in such a way, following the direction of the grooves and oriented in parallel around the major axis of the cell body (Figure 8 (D) and (F), respectively). The control surface did not induce any directional organization of the immunostained myofilaments, and cells displayed a random disposition of F-actin and myosin fibers across the cytoplasm (Figure 8 (C) and (E), respectively). Similarly, most cells showed troponin T oriented and aligned according to the direction of underlying grooves (Figure 8 (B)) while cells from control group, in some cases, exhibited a circular and peripheral arrangement of troponin T and a central area without a defined orientation pattern (Figure 8 (A)). The regularly striated pattern and the more uniaxial arrangement of α-actinin observed from hiPSC-CMs cultured on patterned PET (Figure 9 (B)) reflected the organization of F-actin and myosin light chain-2, whereas without the presence of a microstructured surface, α-actinin was organized in multiple directions and presented an irregularly striated pattern (Figure 9 (A)). Despite the distinct alignment of sarcomeric α-actinin observed between control and patterned PET, cells from both experimental groups showed sarcomere lengths of 1.61 ± 0.22 and 1.62 ± 0.27 μm, respectively (Figure 9).

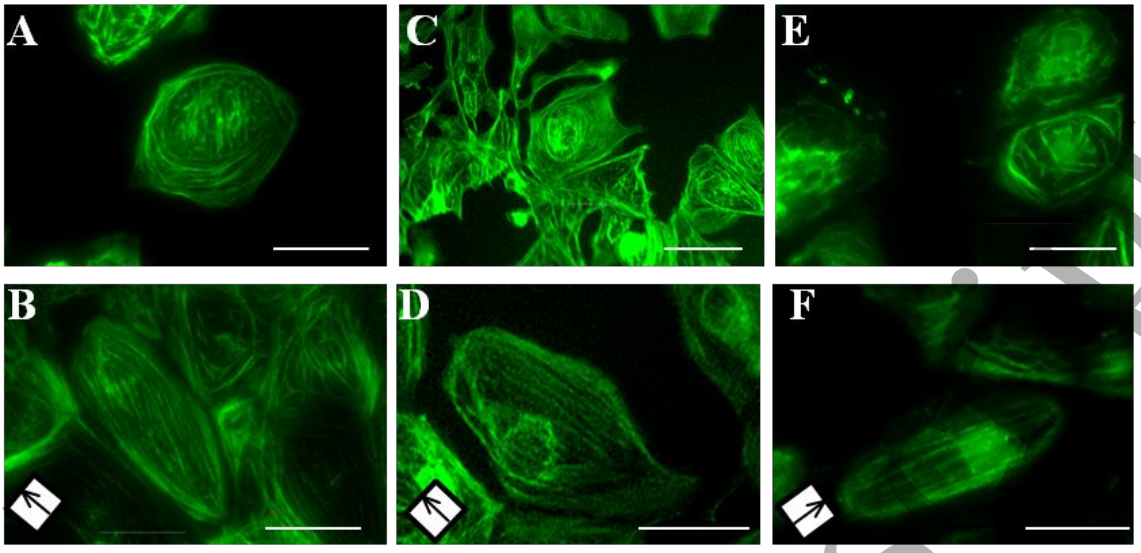

Figure 8. Immunocytochemistry. Representative fluorescent images of hiPSC-CMs grown on control (A, C, E) or DLIP-R2R-modified PET (B, D, F) showing distinct myofibrils arrangement and cell morphology. Troponin (A, B); F-actin (C, D); myosin light chain-2 (E, F). The arrow inside the box indicates the direction of the grooves. Scale bar: 50 μm.

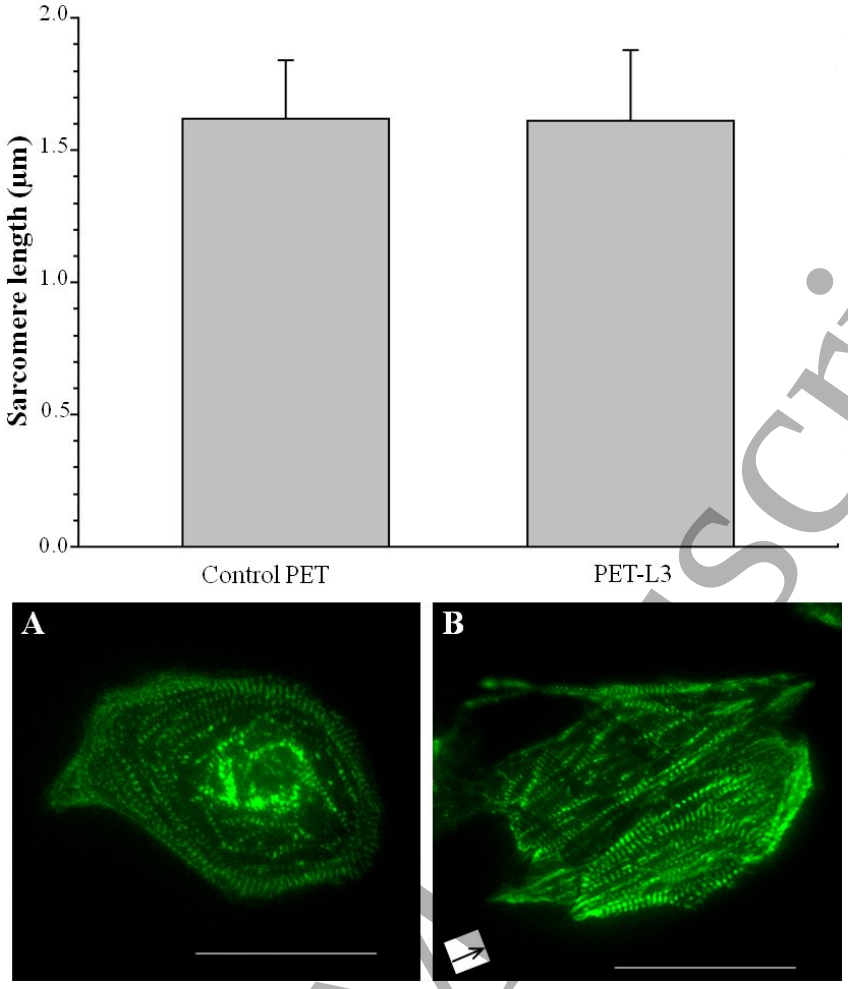

Figure 9. Top: Sarcomere length (µm) from hiPSC-CMs cultured on control or DLIP-R2R-modified PET. Bottom: immunostained images showing distinct organization of sarcomeric alpha-actinin from control (A) and DLIP-R2R-modified PET (B). The arrow inside the box indicates the direction of the grooves. Scale bar: 50 µm.

3.5 Calcium transient measurements

The spontaneous and electrically stimulated contractile activities of hiPSC-CMs were evaluated. Cells were loaded with the Ca^{2+}-sensitive fluorescent indicator Fluo-4, and the luminous signals were recorded and processed to generate maps of fluorescence intensity prior to estimating calcium transient parameters. Representative intensity maps are displayed in Figure 10, and the kinetic parameters obtained are schematically represented in Figure 11 (A) and summarized in Table 2.

Compared to the control group, hiPSC-CMs conditioned on patterned PET presented spontaneous transients showing an overall time reduction of all measured parameters (Table 2, top), except for t_{peak}, which was equal for both experimental groups. The values of dct and pw_{50} were 24% and 25% lower ($P < 0.05$), respectively, and the decay rate was approximately 50% higher ($P < 0.05$) than that of the control cells.

To further explore cell functionality in response to growth on the patterned surface, hiPSC-CMs were exposed to electric field stimulation to test the triggered contractile activity. Concerning all parameters evaluated, cells grown on patterned PET showed calcium transients shorter than those grown on non-patterned PET (Table 2, bottom). The largest difference registered was t_{peak}, with a 46% time reduction ($P < 0.001$). The values of dct and pw_{50} were 28% and 30% lower ($P < 0.001$), respectively, and the transient decay rate was 38% higher ($P < 0.001$) than that observed in the control group (Figure 11 (B)). Representative graphs of fluorescence intensity as a function of time obtained with electrically stimulated hiPSC-CMs are shown in Figure 11 (C) and (D).

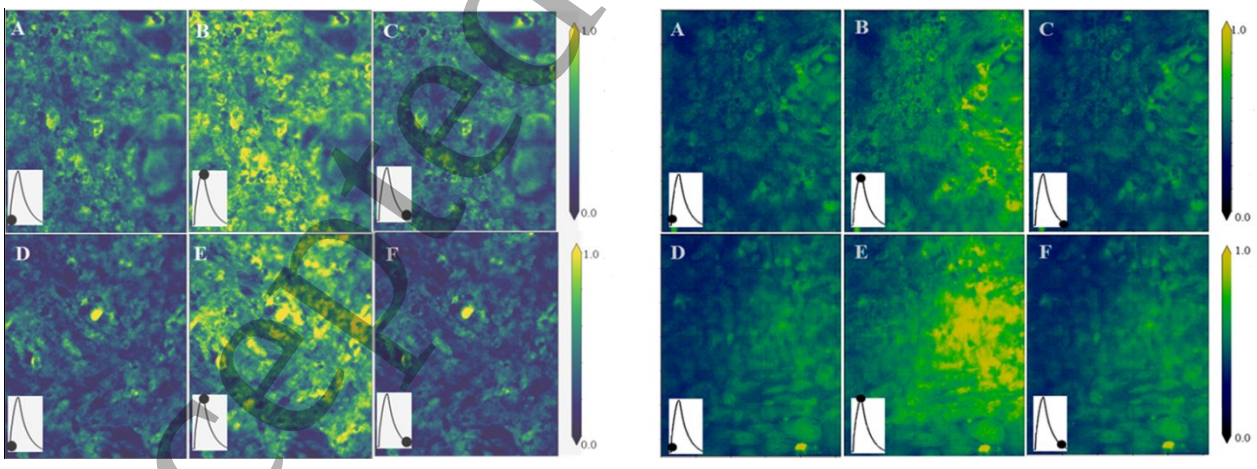

Figure 10. Representative maps of relative fluorescence intensity from non-stimulated (spontaneous) contractile activity (left) and electrically stimulated contractile activity (right) of

hiPSC-CMs cultures. Top frames (A, B, C) are intensity maps from control PET; bottom frames (D, E, F) are from hiPSC-CMs conditioned on patterned PET. The box inside each frame schematically indicates the phase (initial, peak and final) of the transient during recording in relation to the calcium transient. Scale bar: normalized fluorescent intensity.

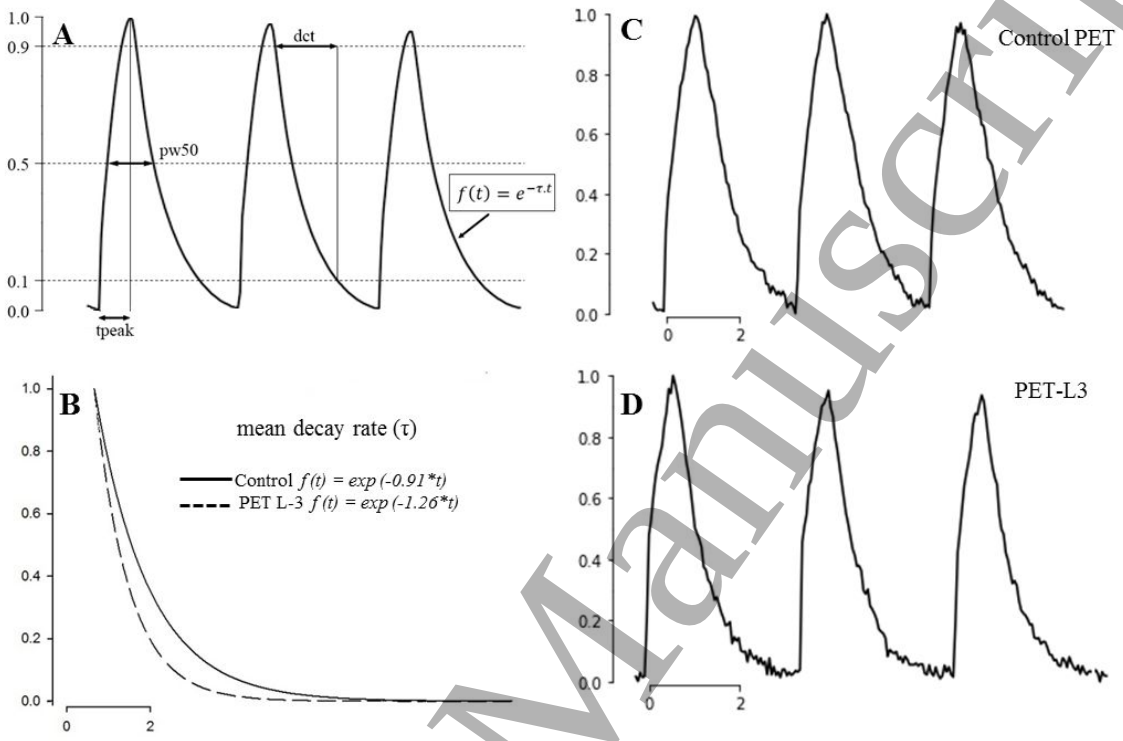

Figure 11. (A), schematic depiction of kinetic parameters measured from calcium transients: t_{peak}, pw_{50}, dct and decay rate. (B), mean decay rate of electrically stimulated hiPSC-CMs grown on control or PET-L3 surfaces. (C) and (D), representative graphics of control and patterned PET, respectively, displaying fluorescence intensity as a function of time obtained with electrically stimulated cells.

Table 2. Kinetic parameters from spontaneous (top) and stimulated (bottom) calcium fluctuations. ($^{\#}$) and (*) indicate statistical significance at $P < 0.05$ and $P < 0.001$, respectively. Values are shown in seconds and presented as median ± SD.

Spontaneous calcium fluctuations				
	t_{peak}	dct	pw_{50}	decay rate (τ)
Control PET	1.51 ± 0.30	2.0 ± 0.08	1.58 ± 0.05	0.77 ± 0.11
PET-L3	1.51 ± 0.30	1.52 ± 0.03$^{\#}$	1.18 ± 0.04$^{\#}$	1.14 ± 0.25$^{\#}$

Stimulated calcium fluctuations				
	t_{peak}	dct	pw_{50}	decay rate (τ)
Control PET	1.24 ± 0.37	1.72 ± 0.26	1.51 ± 0.18	0.91 ± 0.17
PET-L3	0.66 ± 0.11*	1.23 ± 0.25*	1.06 ± 0.15*	1.26 ± 0.18*

4. Discussion

We investigated the *in vitro* effects of surface micropatterning, obtained using a high-throughput technique in cell morphology, alignment, sarcomere assembly, and calcium transients. Cell alignment, aspect ratio, circularity index, spreading area, sarcomeric myofibrils assembly, sarcomere length, and calcium fluctuations were analyzed.

4.1 *DLIP and R2R hot embossing on PET*

Different techniques, such as hot/UV embossing, photolithography, and laser-based structuring have been used to engineer surface topographies on a variety of materials [35]. In this study, we developed a surface modification system based on the sequential use of DLIP and R2R hot embossing for PET sheets.

There are few alternatives to generate large numbers of hiPSC-CMs necessary for high-throughput applications. For large-scale production, hot embossing is one of the

most used methods because it provides low-cost, high-resolution, and high-throughput replication of structures at the micro-and nanoscale [36]. Common methods used to produce embossing molds, including photolithography, micromachining, electroplating, and etching, have drawbacks such as high cost, time consumption, multiple processing steps, resolution limitations, and lack of an accurate dimension control [37].

Our original proposed technique of laser ablation for patterning, in a one-step method, a cylindrical metal stamp and using this in roll-to-roll hot embossing of PET is capable of producing square meters of patterned polymeric surface with a processing throughput of 7.5 m^2 min^{-1}. The sequential combination of direct laser ablation and hot embossing makes it possible to produce large amounts of patterned PET sheets in the low micrometer range and is suitable for conditioning hiPSC-CMs, at a relatively low cost and high resolution.

Furthermore, the relationship between the specific surface topography and cell behavior was evaluated to determine the validity of the method. The line-like pattern with 3 μm spaced grooves was selected considering that it was previously demonstrated that this feature size can be accurately reproduced on PET foils [38] and based on preliminary experiments showing that hiPSC-CMs can respond to grooves of this size (data not shown). This approach may be employed for the surface functionalization of other suitable polymeric materials with biomedical relevance, as well as to introduce different topographic features, such as pillar- and hole-like [35] and line-like patterns. This methodology is able to generate geometric features ranging from the upper nano- to low micro-scale, which are likely to expand its applications to other cell types or culture protocols in tissue-engineering efforts in the production of other tissues such as bone or skin.

4.2 Cell alignment and anisotropic morphology on patterned PET

Mature cardiomyocytes are longitudinally aligned with well-organized myofibrils, while cultured hiPSC-CMs do not have a defined orientation and display a disorganized arrangement of myofibrils [39]. HiPSC-CMs do not show proper alignment in 2D cultures [2] unless topographical modifications are introduced to the culturing surfaces [40]. It has been reported that the presence of parallel micro-and nanogrooves on the surface induces similar physiological cellular alignment [41] and may be used for pre-conditioning hiPSC-CMs before their application in cardiac tissue engineering. Our results of cell orientation indicate a significant proportion (50%) of aligned cells in response to DLIP-R2R-modified PET.

Cellular alignment is strongly correlated with an increase in cell elongation in different cell types [42]. It is known that native adult CMs are rod-shaped, more elongated, and present lower circularity index and higher levels of myofibrils organization than fetal CMs and hiPSC-CMs [2,4]. Thus, elongation measurements are used to quantify the development of morphological anisotropy of hiPSC-CMs and may indicate structural maturity *in vitro* [40]. Our results show that hiPSC-CMs cultured on patterned PET not only aligned to the groove direction at a relevant proportion but also had a 34% decrease in aspect ratio and 11% decrease in circularity index, indicating that cells exhibited a more elongated and anisotropic morphology. The length of an adult human CM lies between 60 and 140 μm, and the cell width is between 17 and 25 μm [43]. Thus, aspect ratio values lower than 0.28 are expected for mature CM [44]. Cells from control PET showed mean length and width of 63 ± 18 and 34 ± 12 μm, respectively, with an aspect ratio of 0.54 ± 0.15. Cells cultured on patterned PET presented major and minor axes of 65 ± 20 and 23 ± 7 μm, respectively, resulting in an aspect ratio of 0.35 ± 0.16, which is higher than the reference value reported for mature CMs, but closer than the control group.

The maturity of hiPSC-CMs can be divided in "early" and "late" developmental phases. Early phase hiPSC-CMs (around 30 days post-induction) have a rounded morphology with 400-500 μm^2 surface area. After this initial period, morphological changes occur, such as an increase in the spreading area resulting in cells within the range of 600-1700 μm^2 [45, 46]. Cells grown on non-modified PET spread out in all directions, without any directional preference, and presented a spreading mean area of 1288 μm^2 (Figure 7). HiPSC-CMs cultured on patterned PET responded distinctly and exhibited a mean area of 904 μm^2. This reduction can be attributed to the contact guidance effect promoted by the topography. We observed that these cells adopted the direction of the grooves (Figure 4 (B)) as the preferred way to launch and stabilize their membrane protrusions during the adhesion process. It is likely that this spatial restriction partly limited the lateral growth of the cell, resulting in cells with a smaller spreading area.

4.3 Myofibrils alignment and sarcomere length

A typical feature of adult cardiomyocytes is their elongated shape, with one long axis along which myofibrils are regularly arranged, leading to the characteristic striation pattern [47]. Thus, the foetal-like resemblance of immature hiPSC-CMs, especially if the sarcomere structure is considered, limits the potential for clinical application [45, 48], considering that the lack of a directional organization of myofibrils results in poor sarcomeric assembly and, ultimately, a weaker contractile force [49, 50]. Our results showed that hiPSC-CMs cultured on patterned PET exhibited a regular striation pattern of α-actinin and an anisotropic alignment of F-actin, myosin light chain-2, and troponin T, according to the direction of the underlying grooves, which resulted in a more uniaxial orientation of the myofibrils.

Besides myofibrils organization, sarcomere length is also associated with force production in cell contractions [51, 52]; thus, it is usually evaluated as an indicator of hiPSC-CMs sarcomeric structural maturity. It has been reported that mature cardiomyocytes have sarcomere lengths within the range of 1.8-2.2 μm [40, 53]. Our results show that hiPSC-CMs cultured on unmodified or patterned PET had mean sarcomere lengths of 1.6 μm, which indicates that hiPSC-CMs responded to patterned PET at the level of myofibrils alignment, but not at the level of sarcomere length. Nevertheless, the ability of the surface pattern to positively influence the assembly of sarcomeric proteins makes the DLIP-R2R hot embossing a suitable technique to produce topographies capable of instructing cell morphology and myofibrils alignment, which can be used to precondition hiPSC-CMs for further use in different applications such as drug screening and disease modeling.

4.4 Ca^{2+} transients – contractile activity of hiPSC-CM on DLIP-R2R-modified PET

We performed functional assays to evaluate the ability of patterned PET to affect calcium handling. We observed a reduction in calcium decay kinetics parameters (decay time, pw_{50}, and decay rate), suggesting faster Ca^{2+} reuptake in these cells. Considering the decay rate, it is noticeable that cells from the structured PET group showed a Ca^{2+} decay rate nearly 50% faster than the control group, indicating faster Ca^{2+} removal mechanisms.

Cell functionality was further investigated by analyzing the contractile activity triggered by electrical stimuli. Under electrical pacing, hiPSC-CMs grown on patterned PET not only presented faster Ca^{2+} recycling, indicated by lower values of dct and pw_{50}, but also exhibited a significantly faster Ca^{2+} release, as indicated by the 46% decrease in t_{peak} measurement. Additionally, the increase of 38% in decay rate illustrates the positive

influence of the cell-surface interaction in Ca^{2+} removal dynamics, leading to shorter transients and, ultimately, in more efficient calcium handling.

5. Conclusions

In this study, we showed that microtopography produced by DLIP in conjunction with R2R-NIL on the PET surface induced changes in hiPSC-CMs morphology, alignment, sarcomeric myofibrils assembly, and calcium handling. These phenotypic changes are associated with structural and functional maturation aspects that are clinically relevant for the eventual production of myocardial tissue implants. This methodology is easily scalable and can be implemented at a relatively low cost and high throughput. Particularly, we demonstrated that the combination of DLIP and R2R-NIL can yield a surface processing throughput of 7.5 m^2 min^{-1} on PET foils. Our results indicate the feasibility of using DLIP and nanoimprint lithography to create microtopography features that may influence some of the maturation aspects of hiPSC-CMs on 2D PET surfaces.

In summary, DLIP/R2R hot embossing of polymeric substrates is a cost-effective and scalable technique for hiPSC-CM that may contribute to morphological remodeling and functional maturation with potential for scaling the production of these cells in research, pharmaceutical industry, and clinical applications.

Acknowledgements

I.N.C., I.A.C, and L.R.X.C acknowledge the support of FAPESP (12/50283-6), Finep (1253/13), and National Council for Scientific and Research Development (CNPq) (467270/2014-7 and 311191/2017-7). M.S. acknowledges the support of the Alexander von Humboldt Foundation. The work of A.F.L. was carried out in the framework of the

Reinhart Koselleck project (LA2513_7-1), supported by the German Research Foundation (German: Deutsche Forschungsgemeinschaft DFG). This project was also funded by the European Regional Development Fund (ERDF) and co-financed under taxation on the basis of the budget adopted by the members of the Saxon State Parliament.

Author Contributions

Conceptualization: I.N.C., I.A.C., and A.F.L. Methodology: L.R.X.C., M.S., A.R., R.D.L., M.C.A. Writing-original draft preparation: L.R.X.C., I.N.C., A.F.L. Writing-review and editing: L.R.X.C., I.N.C., I.A.C., M.S., A.F.L. Supervision: I.N.C., A.F.L.

Data availability

The raw data required to reproduce these findings is available: https://doi.org/10.5061/dryad.v9s4mw6wq

References

[1] Ermis, M., Antmen, E., Hasirci, V., 2018. Micro and Nanofabrication methods to control cell-substrate interactions and cell behavior: A review from the tissue engineering perspective. Bioactive Materials 3, 355–369. https://doi.org/10.1016/j.bioactmat.2018.05.005

[2] Di Baldassarre, A., Cimetta, E., Bollini, S., Gaggi, G., Ghinassi, B., 2018. Human-Induced Pluripotent Stem Cell Technology and Cardiomyocyte Generation: Progress and Clinical Applications. Cells 7, 48. https://doi.org/10.3390/cells7060048

[3] Fujita, J., Tohyama, S., Kishino, Y., Okada, M., Morita, Y., 2019. Concise Review: Genetic and Epigenetic Regulation of Cardiac Differentiation from Human Pluripotent Stem Cells: Molecular Mechanisms of Cardiac Differentiation. Stem Cells 37, 992–1002. https://doi.org/10.1002/stem.3027

[4] Jiang, Y., Park, P., Hong, S.-M., Ban, K., 2018. Maturation of Cardiomyocytes Derived from Human Pluripotent Stem Cells: Current Strategies and Limitations. Molecules and Cells 41, 613–621. https://doi.org/10.14348/MOLCELLS.2018.0143

[5] Tan, S.H., Ye, L., 2018. Maturation of Pluripotent Stem Cell-Derived Cardiomyocytes: a Critical Step for Drug Development and Cell Therapy. J. of

Cardiovasc. Trans. Res. 11, 375–392. https://doi.org/10.1007/s12265-018-9801-5

[6] Ribeiro, A.J.S., Ang, Y.-S., Fu, J.-D., Rivas, R.N., Mohamed, T.M.A., Higgs, G.C., Srivastava, D., Pruitt, B.L., 2015. Contractility of single cardiomyocytes differentiated from pluripotent stem cells depends on physiological shape and substrate stiffness. Proc Natl Acad Sci USA 112, 12705–12710. https://doi.org/10.1073/pnas.1508073112

[7] Novak, A., Barad, L., Zeevi-Levin, N., Shick, R., Shtrichman, R., Lorber, A., Itskovitz-Eldor, J., Binah, O., 2012. Cardiomyocytes generated from CPVTD307H patients are arrhythmogenic in response to β-adrenergic stimulation. Journal of Cellular and Molecular Medicine 16, 468–482. https://doi.org/10.1111/j.1582-4934.2011.01476.x

[8] Sun, N., Yazawa, M., Liu, J., Han, L., Sanchez-Freire, V., Abilez, O.J., Navarrete, E.G., Hu, S., Wang, L., Lee, A., Pavlovic, A., Lin, S., Chen, R., Hajjar, R.J., Snyder, M.P., Dolmetsch, R.E., Butte, M.J., Ashley, E.A., Longaker, M.T., Robbins, R.C., Wu, J.C., 2012. Patient-Specific Induced Pluripotent Stem Cells as a Model for Familial Dilated Cardiomyopathy. Science Translational Medicine 4, 130ra47-130ra47. https://doi.org/10.1126/scitranslmed.3003552

[9] Hooks, D.A., Trew, M.L., Caldwell, B.J., Sands, G.B., LeGrice, I.J., Smaill, B.H., 2007. Laminar Arrangement of Ventricular Myocytes Influences Electrical Behavior of the Heart. Circulation Research 101. https://doi.org/10.1161/CIRCRESAHA.107.161075

[10] Parker, K.K., Ingber, D.E., 2007. Extracellular matrix, mechanotransduction and structural hierarchies in heart tissue engineering. Phil. Trans. R. Soc. B 362, 1267–1279. https://doi.org/10.1098/rstb.2007.2114

[11] Litowczenko, J., Maciejewska, B.M., Wychowaniec, J.K., Kościński, M., Jurga, S., Warowicka, A., 2019. Groove-patterned surfaces induce morphological changes in cells of neuronal origin. J Biomed Mater Res 107, 2244–2256. https://doi.org/10.1002/jbm.a.36733

[12] Babaliari, E., Kavatzikidou, P., Angelaki, D., Chaniotaki, L., Manousaki, A., Siakouli-Galanopoulou, A., Ranella, A., Stratakis, E., 2018. Engineering Cell Adhesion and Orientation via Ultrafast Laser Fabricated Microstructured Substrates. IJMS 19, 2053. https://doi.org/10.3390/ijms19072053

[13] Schieber, R., Lasserre, F., Hans, M., Fernández-Yagüe, M., Díaz-Ricart, M., Escolar, G., Ginebra, M.-P., Mücklich, F., Pegueroles, M., 2017. Direct Laser Interference Patterning of CoCr Alloy Surfaces to Control Endothelial Cell and Platelet

Response for Cardiovascular Applications. Adv. Healthcare Mater. 6, 1700327. https://doi.org/10.1002/adhm.201700327

[14] Dolatshahi-Pirouz, A., Nikkhah, M., Kolind, K., Dokmeci, M.R., Khademhosseini, A., 2011. Micro- and Nanoengineering Approaches to Control Stem Cell-Biomaterial Interactions. JFB 2, 88–106. https://doi.org/10.3390/jfb2030088

[15] Maxime D. Guillemette., Emmanuel Roy., François A. Auger., Teodor Veres. 2011. Rapid isothermal substrate microfabrication of a biocompatible thermoplastic elastomer for cellular contact guidance. Acta Biomaterialia 7, 2492-2498. doi:10.1016/j.actbio.2011.02.019

[16] Takahashi, H and Okano, T., 2015. Cell Sheet-Based Tissue Engineering for Organizing Anisotropic Tissue Constructs Produced Using Microfabricated Thermoresponsive Substrates. Advanced Healthcare Materials 4, 2388–2407. https://doi.org/10.1002/adhm.201500194.

[17] Cortella, L.R.X., Cestari, I.A., Guenther, D., Lasagni, A.F., Cestari, I.N., 2017. Endothelial cell responses to castor oil-based polyurethane substrates functionalized by direct laser ablation. Biomed. Mater. 12, 065010. https://doi.org/10.1088/1748-605X/aa8353

[18] Langheinrich, D., Yslas, E., Broglia, M., Rivarola, V., Acevedo, D., Lasagni, A., 2012. Control of cell growth direction by direct fabrication of periodic micro- and submicrometer arrays on polymers. J. Polym. Sci. B Polym. Phys. 50, 415–422. https://doi.org/10.1002/polb.23017

[19] Alamri, S., Krupop, B., Steege, T., Aguilar Morales, A.I., Lang, V., Storm, S., Schell, F., Zwahr, C., Kracht, C., Bieda, M., Voisiat, B., Klotzbach, U., Lasagni, A.F., Kunze, T., 2019. Quo Vadis surface functionalization: How direct laser interference patterning tackle productivity and flexibility in industrial applications, in: Klotzbach, U., Kling, R., Watanabe, A. (Eds.), Laser-Based Micro- and Nanoprocessing XIII. Presented at the Laser-based Micro- and Nanoprocessing XIII, SPIE, San Francisco, United States, p. 27. https://doi.org/10.1117/12.2514209

[20] Lang, V., Rank, A., Lasagni, A.F., 2017a. Direct laser interference patterning of metallic sleeves for roll-to-roll hot embossing, in: Klotzbach, U., Washio, K., Kling, R. (Eds.). Presented at the SPIE LASE, San Francisco, California, United States, p. 100920T. https://doi.org/10.1117/12.2252623

[21] Rank, A., Lang, V., Voisiat, B., Lasagni, A.F., 2019. "Roll-to-roll hot embossing process: A way to scale up the fabrication speed of micro-nano structures formed by

direct laser interference patterning (Conference Presentation)", Proc. SPIE 10906, Laser-based Micro- and Nanoprocessing XIII, 109060V; https://doi.org/10.1117/12.2509386

[22] Lang, V., Rank, A., Lasagni, A.F., 2017b. Large Area One-Step Fabrication of Three-Level Multiple-Scaled Micro and Nanostructured Nickel Sleeves for Roll-to-Roll Hot Embossing: Large Area Fabrication of Three-Level microstructures. Adv. Eng. Mater. 19, 1700126. https://doi.org/10.1002/adem.201700126

[23] Lasagni, A.F., Lang, V., Rank, A., Voisiat, B., 2018. Micro-nano structuring of sleeves for roll-to-roll embossing processes using Direct Laser Interference Patterning , Proceedings of LPM 2018, The 19th International Symposium on Laser Precision Microfabrication, Edinburgh, UK).

[24] Leitgeb, M., Nees, D., Ruttloff, S., Palfinger, U., Götz, J., Liska, R., Belegratis, M.R., Stadlober, B., 2016. Multilength Scale Patterning of Functional Layers by Roll-to-Roll Ultraviolet-Light-Assisted Nanoimprint Lithography. ACS Nano 10, 4926–4941. https://doi.org/10.1021/acsnano.5b07411

[25] Estevam-Alves, R., Günther, D., Dani, S., Eckhardt, S., Roch, T., Mendonca, C.R., Cestari, I.N., Lasagni, A.F., 2016. UV Direct Laser Interference Patterning of polyurethane substrates as tool for tuning its surface wettability. Applied Surface Science 374, 222–228. https://doi.org/10.1016/j.apsusc.2015.11.119

[26] Arana, M.C., Lahuerta, R.D., Cortella, L.R.X., Mazzetto, M., Soldera, M., Lasagni, A.F., Cestari, I.N., Cestari. I.A., 2020. Experimental Apparatus for Evaluation of Calcium Fluctuations in Cardiomyocytes Derived from Human-Induced Pluripotent Stem Cells. IFMBE Proceedings, Vol. 83, TeodianoFreire Bastos-Filho et al. (Eds): XXVII Brazilian Congress on Biomedical Engineering, 978-3-030-70600-5, 509957_1_En, (Chapter 31).

[27] Rossum, G V., Drake F., 2009. Python 3 Reference Manual. Scotts Valley, CA: CreateSpace.

[28] Van der Walt, S., Colbert, S.C., Varoquaux, G et al., 2011. The NumPy array: a structure for efficient numerical computation. Comput Sci Eng 13:22–30 DOI 10.1109/MCSE.2011.37

[29] Hunter, J.D et al. 2007. Matplotlib: A 2D graphics environment. Comput Sci Eng 9:90–95 DOI 10.1109/MCSE.2007.55

[30] Olson, J.S. 1963. "Energy storage and the balance of producers and decomposers in ecological systems." Ecology 44.2 (1963): 322-331. https://doi.org/10.2307/1932179

[31] Newville, M. et al., 2016. "LMFIT: Non-linear least-square minimization and curve-fitting for Python." Astrophysics Source Code Library: ascl-1606. DOI:10.5281/zenodo.11813

[32] Lourakis, M.I.A., 2005. "A brief description of the Levenberg-Marquardt algorithm implemented by levmar." Foundation of Research and Technology 4.1: 1-6. http://web.eecs.utk.edu/~mjr/ECE505/Miscellaneous/levmar.pdf

[33] Badie, N., Satterwhite, L., Bursac, N., 2009. A Method to Replicate the Microstructure of Heart Tissue In Vitro Using DTMRI-Based Cell Micropatterning. Ann Biomed Eng 37, 2510–2521. https://doi.org/10.1007/s10439-009-9815-x

[34] Khan, M., Xu, Y., Hua, S., Johnson, J., Belevych, A., Janssen, P.M.L., Gyorke, S., Guan, J., Angelos, M.G., 2015. Evaluation of Changes in Morphology and Function of Human Induced Pluripotent Stem Cell Derived Cardiomyocytes (HiPSC-CMs) Cultured on an Aligned-Nanofiber Cardiac Patch. PLoS ONE 10, e0126338. https://doi.org/10.1371/journal.pone.0126338

[35] Fu, Y., Soldera, M., Wang, W., Milles, S., Deng, K., Voisiat, B., Nielsch, K., Lasagni, A.F., 2020. Wettability control of polymeric microstructures replicated from laser-patterned stamps. Sci Rep 10, 22428. https://doi.org/10.1038/s41598-020-79936-1

[36] Wu, C.-L., Sung, C.-K., Yao, P.-H., Chen, C.-H., 2013. Sub-15 nm linewidth gratings using roll-to-roll nanoimprinting and plasma trimming to fabricate flexible wire-grid polarizers with low colour shift. Nanotechnology 24, 265301. https://doi.org/10.1088/0957-4484/24/26/265301

[37] Peng, L., Deng, Y., Yi, P., Lai, X., 2014. Micro hot embossing of thermoplastic polymers: a review. J. Micromech. Microeng. 24, 013001. https://doi.org/10.1088/0960-1317/24/1/013001

[38] Rank, A., Lang, V., Lasagni, A.F., 2017. High-Speed Roll-to-Roll Hot Embossing of Micrometer and Sub Micrometer Structures Using Seamless Direct Laser Interference Patterning Treated Sleeves: Embossing of Micrometer and Sub Micrometer Structures. Adv. Eng. Mater. 19, 1700201. https://doi.org/10.1002/adem.201700201

[39] Xu, C., Wang, L., Yu, Y., Yin, F., Zhang, X., Jiang, L., & Qin, J. (2017). Bioinspired onion epithelium-like structure promotes the maturation of cardiomyocytes derived from human pluripotent stem cells. Biomaterials Science, 5(9), 1810–1819. https://doi.org/10.1039/C7BM00132K.

[40] Carson, D., Hnilova, M., Yang, X., Nemeth, C.L., Tsui, J.H., Smith, A.S.T., Jiao, A., Regnier, M., Murry, C.E., Tamerler, C., Kim, D.-H., 2016. Nanotopography-

Induced Structural Anisotropy and Sarcomere Development in Human Cardiomyocytes Derived from Induced Pluripotent Stem Cells. ACS Appl. Mater. Interfaces 8, 21923–21932. https://doi.org/10.1021/acsami.5b11671

[41] Jiao, A., Trosper, N.E., Yang, H.S., Kim, J., Tsui, J.H., Frankel, S.D., Murry, C.E., Kim, D.-H., 2014. Thermoresponsive Nanofabricated Substratum for the Engineering of Three-Dimensional Tissues with Layer-by-Layer Architectural Control. ACS Nano 8, 4430–4439. https://doi.org/10.1021/nn4063962

[42] Aubin, H., Nichol, J.W., Hutson, C.B., Bae, H., Sieminski, A.L., Cropek, D.M., Akhyari, P., Khademhosseini, A., 2010. Directed 3D cell alignment and elongation in microengineered hydrogels. Biomaterials 31, 6941–6951. https://doi.org/10.1016/j.biomaterials.2010.05.056

[43] Tracy, R.E., Sander, G.E., 2011. Histologically Measured Cardiomyocyte Hypertrophy Correlates with Body Height as Strongly as with Body Mass Index. Cardiology Research and Practice 2011, 1–9. https://doi.org/10.4061/2011/658958

[44] Huethorst, E., Hortigon, M., Zamora-Rodriguez, V., Reynolds, P.M., Burton, F., Smith, G., Gadegaard, N., 2016. Enhanced Human-Induced Pluripotent Stem Cell Derived Cardiomyocyte Maturation Using a Dual Microgradient Substrate. ACS Biomater. Sci. Eng. 2, 2231–2239. https://doi.org/10.1021/acsbiomaterials.6b00426

[45] Robertson, C., Tran, D.D., George, S.C., 2013. Concise Review: Maturation Phases of Human Pluripotent Stem Cell-Derived Cardiomyocytes. STEM CELLS 31, 829–837. https://doi.org/10.1002/stem.1331

[46] Yang, X., Pabon, L., Murry, C.E., 2014. Engineering Adolescence: Maturation of Human Pluripotent Stem Cell–Derived Cardiomyocytes. Circ Res 114, 511–523. https://doi.org/10.1161/CIRCRESAHA.114.300558

[47] Silbernagel, N., Körner, A., Balitzki, J., Jaggy, M., Bertels, S., Richter, B., Hippler, M., Hellwig, A., Hecker, M., Bastmeyer, M., Ullrich, N.D., 2020. Shaping the heart: Structural and functional maturation of iPSC-cardiomyocytes in 3D-micro-scaffolds. Biomaterials 227, 119551. https://doi.org/10.1016/j.biomaterials.2019.119551

[48] Laflamme, M.A., Chen, K.Y., Naumova, A.V., Muskheli, V., Fugate, J.A., Dupras, S.K., Reinecke, H., Xu, C., Hassanipour, M., Police, S., O'Sullivan, C., Collins, L., Chen, Y., Minami, E., Gill, E.A., Ueno, S., Yuan, C., Gold, J., Murry, C.E., 2007. Cardiomyocytes derived from human embryonic stem cells in pro-survival factors enhance function of infarcted rat hearts. Nat Biotechnol 25, 1015–1024. https://doi.org/10.1038/nbt1327

[49] Snir, M., Kehat, I., Gepstein, A., Coleman, R., Itskovitz-Eldor, J., Livne, E., Gepstein, L., 2003. Assessment of the ultrastructural and proliferative properties of human embryonic stem cell-derived cardiomyocytes. American Journal of Physiology-Heart and Circulatory Physiology 285, H2355–H2363. https://doi.org/10.1152/ajpheart.00020.2003

[50] Davis, R.P., Casini, S., Hoekstra, M., Remme, C.A., Dambrot, C., Salvatori, D., Oostwaard, D.W., Wilde, A.A.M., Bezzina, C.R., Verkerk, A.O., Freund, C., Mummery, C.L., 2012. Cardiomyocytes Derived From Pluripotent Stem Cells Recapitulate Electrophysiological Characteristics of an Overlap Syndrome of Cardiac Sodium Channel Disease. Circulation 125, 3079-3091. DOI: 10.1161/CIRCULATIONAHA.111.066092

[51] Hibberd, M.G., Jewell, B.R., 1982. Calcium- and length-dependent force production in rat ventricular muscle. The Journal of Physiology 329, 527–540. https://doi.org/10.1113/jphysiol.1982.sp014317

[52] Kentish, J.C., ter Keurs, H.E., Ricciardi, L., Bucx, J.J., Noble, M.I., 1986. Comparison between the sarcomere length-force relations of intact and skinned trabeculae from rat right ventricle. Influence of calcium concentrations on these relations. Circ Res 58, 755–768. https://doi.org/10.1161

[53] Denning, C., Borgdorff, V., Crutchley, J., Firth, K.S.A., George, V., Kalra, S., Kondrashov, A., Hoang, M.D., Mosqueira, D., Patel, A., Prodanov, L., Rajamohan, D., Skarnes, W.C., Smith, J.G.W., Young, L.E., 2016.. Cardiomyocytes from human pluripotent stem cells: From laboratory curiosity to industrial biomedical platform. Biochimica et Biophysica Acta 21, 1863, 1728-1748. http://dx.doi.org/10.1016/j.bbamcr.2015.10.014